CMS Physics Analysis Summary

Contact: cms-pag-conveners-heavyions@cern.ch 2017/02/07

Jet properties in PbPb and pp collisions at $\sqrt{s_{NN}} = 5.02$ TeV

The CMS Collaboration

Abstract

Modifications to high transverse momentum (p_{T}) jets in the quark gluon plasma (QGP) are studied in PbPb and pp collisions at $\sqrt{s_{NN}} = 5.02$ TeV via correlations between jets with $p_{\mathrm{T}} > 120$ GeV and charged particles with $p_{\mathrm{T}} > 0.7$ GeV. This measurement aims to extend results of the same correlations at $\sqrt{s_{NN}} = 2.76$ TeV, which observed significant modification of jet track correlations out to large distances from the jet axis in central PbPb events. This analysis measures correlations in relative pseudorapidity ($\Delta\eta$), relative azimuth ($\Delta\phi$), and relative distance from the jet axis $\Delta r = \sqrt{\Delta\eta^2 + \Delta\phi^2}$. Results are presented as a function of PbPb collision centrality and track p_{T}, providing a differential picture of jet modifications in the medium. Measurements include charged particle densities as a function of distance from jet axis, total charged-particle yields as a function of track-p_{T} (fragmentation functions), and the jet momentum density profile ("jet shape"). This analysis uses data collected with the CMS detector at collision energy $\sqrt{\mathrm{s_{NN}}} = 5.02$ TeV in 2015, corresponding to integrated luminosities of 404 $\mu\mathrm{b}^{-1}$ for PbPb and 27.4 pb^{-1} for pp.

1 Introduction

High transverse momentum (p_{T}) jets are associated with partons produced in the initial hard scatterings of heavy ion collisions, and may be used to probe the properties of the quark gluon plasma (QGP) as they pass through the medium. One example of such response is jet quenching [1], which was observed first at the BNL RHIC [2, 3] and then at the CERN LHC [4–7] via observables including the suppression of high-p_{T} leading track and jet yields in head-on PbPb collisions relative to pp reference data. Using data collected during Run-1 at the LHC, studies have shown that the jet structure is also modified by the medium, as observed via precise measurements of the fragmentation pattern [8, 9] and the distribution of charged-particle transverse momentum ($p_{\mathrm{T}}^{\mathrm{trk}}$) as a function of radial distance from the jet axis [10]. It has also been observed that these modifications extend to large distances in relative pseudorapidity ($\Delta\eta$) and relative azimuth ($\Delta\phi$) with respect to the jet axis [11–13]. Various theoretical models have since attempted to account for these modifications [14–18]. This new measurement aims to extend the previous results at $\sqrt{s_{\mathrm{NN}}}$ = 2.76 TeV to 5.02 TeV, where an increase in jet quenching is expected, and therefore increased jet constituent displacement might be observed.

This analysis uses LHC Run-2 data collected by the CMS Collaboration during 2015, corresponding to integrated luminosities of 404 $\mu\mathrm{b}^{-1}$ for PbPb and 27.4 pb^{-1} for pp. These new data permit measurements of jet properties at a new center-of-mass energy, and allow for the extension of these measurements to larger distances from the jet axis where statistical power was limited in Run-1 pp data. Using correlations between high-p_{T} jets and charged-particle tracks, this analysis presents the distribution of charged particles with respect to the jet axis as a function of relative pseudorapidity ($\Delta\eta$), relative azimuth ($\Delta\phi$), and radial distance $\Delta r = \sqrt{\Delta\eta^2 + \Delta\phi^2}$ from the jet axis, as well as a measurement of the distribution of $p_{\mathrm{T}}^{\mathrm{trk}}$ with respect to the jet axis (known as the "jet shape"). Results are presented differentially as a function of PbPb collision centrality (i.e. the degree of overlap of the colliding nuclei, with head-on collisions defined as "most central") and $p_{\mathrm{T}}^{\mathrm{trk}}$.

2 The CMS detector

The central feature of the CMS apparatus is a superconducting solenoid of 6 m internal diameter, providing a magnetic field of 3.8 T. Within the solenoid volume are a silicon pixel and strip tracker, a lead tungstate crystal electromagnetic calorimeter (ECAL), and a brass and scintillator hadron calorimeter (HCAL), each composed of a barrel and two endcap sections. Two hadronic forward (HF) steel and quartz-fiber calorimeters complement the barrel and endcap detectors, providing coverage to $|\eta| < 5.2$ [19]. In this analysis, the collision centrality is determined using the total sum of transverse energy (E_{T}) from calorimeter towers in the HF region (covering $2.9 < |\eta| < 5.2$). The E_{T} distribution is used to divide the event sample into bins, each representing 0.5% of the total nucleus-nucleus hadronic interaction cross section. A detailed description of centrality determination can be found in Ref. [6].

Jet reconstruction for this analysis relies on calorimeter information from the ECAL and HCAL. For the central region ($|\eta| < 1.6$) in which jets are selected for this analysis, the HCAL cells have widths of 0.087 in both η and ϕ. In the η–ϕ plane, and for $|\eta| < 1.48$, the HCAL cells map on to 5×5 ECAL crystal arrays to form calorimeter towers projecting radially outwards from close to the nominal interaction point. Within each tower, the energy deposits in ECAL and HCAL cells are summed to define the calorimeter tower energies, subsequently used to provide the energies and directions of hadronic jets [20].

Accurate particle tracking is critical for measurements of charged-hadron yields. The CMS

silicon tracker measures charged particles within the pseudorapidity range $|\eta| < 2.5$. It consists of 1,440 silicon pixel and 15,148 silicon strip detector modules. For nonisolated particles of $1 < p_T < 10\,\text{GeV}$ and $|\eta| < 1.4$, the track resolutions are typically 1.5% in p_T and 25–90 (45–150) μm in the transverse (longitudinal) impact parameter [21]. A detailed description of the CMS detector, together with a definition of the coordinate system used and the relevant kinematic variables, can be found in [19].

3 Event selection and Monte Carlo samples

The pp data used in this analysis is selected with a calorimeter energy-based trigger based on the anti-k_t jet-finding algorithm with resolution parameter R = 0.4 (discussed in Sec. 4), which is used to select events containing at least one jet with $p_T > 80$ GeV. This trigger is not prescaled and is fully efficient for events containing offline reconstructed jets with $p_T > 90$ GeV. Two samples of PbPb data are used: a jet-triggered sample used to study the jet-related particle yields, and minimum-bias data sample used for the event mixing technique described in Sec. 5.2. The PbPb jet-triggered sample is obtained using a trigger that selects events containing at least one anti-k_t (R = 0.4) jet with $p_T > 100$ GeV, and is fully efficient for events containing offline reconstructed jets with $p_T > 115$ GeV. In order to avoid contamination from non-collision events, e.g. calorimeter noise and beam-scraping events, the standard vertex and noise filters used for the 2015 CMS heavy-ion data are applied. These selections include restricting to events with at least 3 GeV deposited in each of the HF calorimeters, with a primary reconstructed vertex associated with at least two tracks that falls within 15 cm of the center of the detector along the beam axis ($|v_z| < 15$cm).

In this analysis, Monte Carlo simulations have been principally used for evaluation of reconstruction performance, particularly in the determination of tracking efficiency as well as jet energy response and resolution. These studies primarily use PYTHIA (version 6, tune Z2 [22]) as the hard interaction generator. In order to have reasonable event samples in all jet p_T ranges, different samples are produced with various cut-off values of $\hat{p_T}$. These samples are combined with their corresponding cross-section values as weights. GEANT4 is used for the detector simulation of the generated events [23]. In order to account for effects due to the underlying PbPb events, the hard PYTHIA interactions are embedded into fully simulated minimum-bias PbPb events, generated by HYDJET (Drum5 tune) [24]. This embedded sample simulating jet-triggered PbPb data will be referred to as PYTHIA+HYDJET. In PbPb data, hard probes occur more frequently in more central events due to the large number of binary collisions per nuclear interaction. Since the HYDJET sample is produced as minimum bias PbPb collisions, a centrality-based reweighting is applied to the PYTHIA + HYDJET sample in order to match the centrality distribution of jet-triggered PbPb data. Another reweighting procedure is also performed to match the simulated v_z distributions to the data distributions for both pp and PbPb collisions. Finally, as discussed above, a cross-section weight is applied to different $\hat{p_T}$ samples in order to properly combine them.

4 Jet and track reconstruction

Jet reconstruction in heavy-ion collisions in CMS is performed with an anti-k_t jet algorithm that is encoded in the FastJet framework [25]. This algorithm is similar to the well-known k_t algorithm, except that it uses $1/p_T$ instead of p_T as the weighting factor for the scaled distance. The algorithm is collinear- and infrared-safe, and it produces jets that are circular in y-ϕ space except when jets overlap. In this analysis, individually calibrated ECAL and HCAL towers

are used as input to the anti-k_t jet algorithm, and the algorithm is run with jet-finding radius parameter R = 0.4. In PbPb collisions, underlying event subtraction is performed using a variant of an iterative "noise/pedestal subtraction" technique [26]. In this algorithm, a pedestal function P(η) containing the mean energy and dispersion are calculated in narrow ranges of detector η. The pedestal P(η) is then subtracted from all calorimeter cells. Where this results in non-physical negative energy values for a cell, that cell's energy is set to zero. $\langle \mathrm{E_{cell}} \rangle + \langle \sigma(\mathrm{E_{cell}}) \rangle$ is then subtracted from each cell to compensate for the elimination of negative energy cells. The anti-k_t with radius parameter R = 0.4 is then employed for jet reconstruction. Information about the performance of this algorithm is documented in Ref. [26].

For studies of pp data and PYTHIA MC, charged particles are reconstructed using the same iterative tracking method [21] as in the previous CMS analyses of pp collisions. For PbPb data and PYTHIA+HYDJET, an iterative charged particle reconstruction similar to that of earlier heavy ion analyses [10, 27] is employed, based on hit information from both pixel and silicon strip subdetectors and capable of reconstructing tracks with transverse momentum as low as 0.4 GeV. Tracking efficiency in pp collisions ranges from approximately 80% at 0.5 GeV to 90% or better at 10 GeV and higher. Track reconstruction is more difficult in the heavy ion environment due to the high track multiplicity, and PbPb tracking efficiency ranges from approximately 30% at 0.5 GeV to about 70% at 10 GeV. Corrections for tracking efficiency and related effects are derived as derived as a function of centrality, p_T, η, ϕ, and local charged particle density using PYTHIA simulation for pp tracking and minimum bias PYTHIA+HYDJET for PbPb tracking.

5 Jet-track angular correlations

Jets are selected with the criteria that they have $p_\mathrm{T} > 120$ GeV, and are found within the pseudorapidity interval $|\eta| < 1.6$. Events are studied differentially in collision centrality, with the following bins: 0-10% (most central), 10-30%, 30-50%, and 50-100% (most peripheral). In this inclusive jet selection, it is possible for multiple jets to be selected from the same event, provided that each jet satisfies the selection criteria. Charged tracks in the event with $p_\mathrm{T}^\mathrm{trk}$ above 0.7 GeV are used to construct a two-dimensional relative pseudorapidity ($\Delta\eta = \eta_\mathrm{jet} - \eta_\mathrm{track}$), relative-azimuth ($\Delta\phi = \phi_\mathrm{jet} - \phi_\mathrm{track}$) correlation with respect to the measured jet axis. These correlations measured in various track p_T ranges and normalized by the number of jets in the sample, so that the starting point for this analysis is the per-jet average $\Delta\eta$–$\Delta\phi$ distribution of charged particles about the jet axis for each $p_\mathrm{T}^\mathrm{trk}$ range. For the momentum distribution component of this analysis, correlations are weighted by track transverse momentum on a per-track basis, producing in this case per-jet average $\Delta\eta$–$\Delta\phi$ distribution of charged-particle transverse momentum about the jet axis in the same $p_\mathrm{T}^\mathrm{trk}$ ranges listed above.

5.1 Analysis procedure

After the construction of the initial two-dimensional correlations described above, the remaining analysis procedure consists of the following steps, which will be discussed in detail below:

- A pair-acceptance correction, derived by the "mixed event" method;
- Background subtraction;
- Corrections for jet reconstruction biases: a full simulation-based analysis is conducted to determine and subtract the correlated yield produced by jet-selection bias.

5.2 Pair-acceptance correction

With jet acceptance of $|\eta_{\text{jet}}| < 1.6$, many tracks within $|\Delta\eta| < 2.5$ of a jet will fall outside of the track acceptance of $|\eta_{\text{track}}| < 2.4$, resulting in correlation geometry that falls with increasing $\Delta\eta$. To correct for this pair-acceptance effect, a mixed-event distribution is constructed by correlating jets from the jet-triggered event sample with tracks from a sample of minimum bias events, matched in vertex position (within 1 cm) and collision centrality (within 2.5%), following the technique used for two-particle correlations in Refs. [28–30] and then for jet-track correlations in Refs. [12, 13, 31]. In the following, N_{jets} denotes the number of jets selected as described in a given data sample. The per-jet associated yield is defined as:

$$\frac{1}{N_{\text{jets}}}\frac{\mathrm{d}^2N}{\mathrm{d}\Delta\eta\,\mathrm{d}\Delta\phi} = \frac{ME(0,0)}{ME(\Delta\eta,\Delta\phi)} \times S(\Delta\eta,\Delta\phi). \tag{1}$$

The signal pair distribution, $S(\Delta\eta,\Delta\phi)$, represents the yield of jet-track pairs normalized by N_{jets} from the same event:

$$S(\Delta\eta,\Delta\phi) = \frac{1}{N_{\text{jets}}}\frac{\mathrm{d}^2N^{\text{same}}}{\mathrm{d}\Delta\eta\,\mathrm{d}\Delta\phi}\,. \tag{2}$$

The mixed-event pair distribution,

$$ME(\Delta\eta,\Delta\phi) = \frac{1}{N_{\text{jets}}}\frac{\mathrm{d}^2N^{\text{mix}}}{\mathrm{d}\Delta\eta\,\mathrm{d}\Delta\phi}\,, \tag{3}$$

is constructed to account for pair-acceptance effects, with N^{mix} denoting the number of mixed-event jet-track pairs.

Signal and mixed event correlations are both corrected for tracking efficiencies on a per-track basis, using the efficiency parametrization defined as a function of centrality, $p_{\text{T}}^{\text{trk}}$, η, ϕ, and local charged-particle density. The ratio $ME(0,0)/ME(\Delta\eta,\Delta\phi)$ establishes the correction normalization, with $ME(0,0)$ representing the mixed-event associated yield for jet-track pairs going in approximately the same direction and thus having full pair acceptance. After mixed event correction, jet-particle correlations with respect to the jet axis remain that show a gaussian-like peak confined to the region $|\Delta\eta| < 1.5$ (or narrower), sitting on a large combinatorial and long range-correlated background. To model the long range and uncorrelated underlying event, the region $1.5 < |\Delta\eta| < 2.5$ is projected into the entire $\Delta\phi$ range. This long range distribution is then propagated in $\Delta\eta$ and subtracted in 2D from the signal correlations.

Simulation-based corrections are applied to correlations to account for two biases in jet reconstruction: a bias toward selecting jets with harder fragmentation (affecting PbPb and pp similarly), and a bias toward selecting jets that are found on upward fluctuations in the background (relevant for PbPb only). Jets with harder fragmentation are more likely to be successfully reconstructed than jets with softer fragmentation, resulting in a bias toward the selection of jets with fewer associated tracks in both pp and PbPb data for all track-p_{T} selections studied. Following the method used in [11–13], we derive corrections for this bias by comparing per-jet yields of generated particles correlated to reconstructed jets to per-jet yields of generated particles correlated to generated jets. For pp reference, this correction is derived for each jet selection in PYTHIA-only simulation. To study this effect in PbPb, we consider only generated particles associated with the embedded PYTHIA hard process, excluding the particles associated with the underlying event (which will be used in the next correction for background fluctuation bias).

In PbPb data, there is an additional jet reconstruction bias toward selecting jets that sit on upward fluctuations in the background (since the jet spectrum is steeply falling, more jets on

upward fluctuations are included in the sample than jets on downward fluctuations excluded). To estimate and subtract the contribution to the excess yield due to background fluctuation bias in jet reconstruction, we follow a similar procedure to that outlined in previous CMS studies [12, 13, 32]. We consider correlations in PYTHIA+HYDJET between reconstructed jets and generated particles associated with the HYDJET underlying event, excluding the particles from the embedded hard process. These underlying event particles are found to follow gaussian distributions in $\Delta\eta$ and $\Delta\phi$. In order to avoid propagating low-p_{T} HYDJET fluctuations to the data, the distributions are fit with gaussian functions, and these gaussians fits are applied as the correction to the PbPb data.

6 Systematic uncertainties

A number of sources of systematic uncertainty are considered in the measurement of jet track correlations. These sources include the tracking efficiency, pair acceptance corrections, and background subtraction closure, as well as additional uncertainties arising from jet reconstruction. Where relevant, Monte Carlo simulations to calculate systematic uncertainty related to tracking and jet reconstruction are performed by comparing reconstructed to generated samples from PYTHIA and PYTHIA+HYDJET. Half of the magnitude of the corrections applied for the jet fragmenation and background fluctuation biases (described in Sec. 5.2) is assigned as systematic uncertainty. To conservatively account for the uncertainty associated with the smoothing procedure of gaussian fits to the background fluctuation bias corrections, the error on this fit is included as an additional contribution to the background fluctuation bias uncertainty.

Jet reconstruction-related sources of systematic uncertainty in this analysis include the two reconstruction biases as discussed above, as well uncertainty associated with the jet energy scale (JES) evaluation. We consider three sources of uncertainty on the JES: (1) differences in calorimeter response for quark versus gluon jets, meaning that medium-induced changes in jet flavor could result in either over-correction or under-correction of jet energy and a resulting bias in jet selection (responsible for up to 3% Monte Carlo non-closure for quark and gluon jets); (2) possible differences between data and simulation of up to 4%; (3) uncertainty of up to 2% due to quenching effects not included in our HYDJET simulation. To evaluate how each of these sources of JES uncertainty affects final correlations, we vary jet selection threshold by 5%, and find that this results in up to 2% differences in the final correlations. Together, these three sources therefore comprise a total JES uncertainty within 4%. The tracking efficiency correction uncertainty is estimated from the ratio of corrected reconstructed yields and generated yields by using generator level charged particles as a "truth" reference. The systematic uncertainty from tracking efficiency closure is found to be within 1% in PbPb and 5% in pp collisions. To account for the possible track reconstruction differences in data and simulation, a residual uncertainty in track reconstruction efficiency and fake rate corrections is estimated to be 5% in PbPb and 4% in pp. Since all the measured correlations are studied per-reconstructed jets, the jet reconstruction efficiency does not contribute to the systematic uncertainty of this measurement.

Uncertainty arising from pair-acceptance effects is estimated by considering the sideband asymmetry after dividing by the mixed-event background. Each sideband region of the final $\Delta\eta$ distribution ($-2.5 < \Delta\eta < -1.5$ and $1.5 < \Delta\eta < 2.5$) is separately fit with a horizontal line after background subtraction. The greater of these two deviations from zero is assigned as systematic error, and is found to be within 5% for the lowest track p_{T} bin. Uncertainties resulting from the background subtraction are determined by considering the average point-to-point de-

viation in two parts of the sideband region ($1.5 < |\Delta\eta| < 2.0$ and $2.0 < |\Delta\eta| < 2.5$) after background subtraction. In more central events (0–10%), this background subtraction uncertainty is found to be within 9% for the lowest track p_{T} bin where the background is most significant compared to the signal level, and decreases for less central collisions and for higher p_{T} tracks ($p_{\mathrm{T}}^{\mathrm{trk}} > 2$ GeV/c). The systematic uncertainties from different sources mentioned above are added in quadrature for the final result. Table 1 lists the upper limits of the estimated contributions from the individual sources described above.

Table 1: Systematic uncertainties in the measurement of the jet track correlations in PbPb and pp collisions. The numbers presented in this table summarize typical range of systematic uncertainty as a function of collision centrality. The upper limits of the cited values correspond to uncertainties at lowest $p_{\mathrm{T}}^{\mathrm{trk}}$, and uncertainties decrease with rising $p_{\mathrm{T}}^{\mathrm{trk}}$.

Source	0–10%	10–30%	30–50%	50–100%	ppRef
Background fluctuation bias	0–10%	0–5%	0–2%	0–1%	–
Background fluctuation bias residual	0–2%	0–3%	0–1%	0–1%	–
JFF bias	3–5%	3–4%	3–4%	3–4%	3%
Residual JES	4%	4%	4%	4%	4%
Tracking efficiency uncertainty	1%	1%	1%	1%	1%
Residual tracking efficiency	5%	5%	5%	5%	5%
Pair-acceptance corrections	1–5%	1–4%	1–4%	1–4%	1–2%
Background subtraction	1–9%	0–4%	0–4%	0–3%	0–3%
Total	7–16%	7–11%	7–9%	7–9%	7–8%

7 Results

7.1 Angular distribution of charged-particle yields

Results in this analysis are presented differentially in $p_{\mathrm{T}}^{\mathrm{trk}}$ and PbPb collision centrality, and are compared to pp reference data. Figures 1 and 2 present charged particle yields, differentially in $p_{\mathrm{T}}^{\mathrm{trk}}$, as a function of $\Delta\eta$ and $\Delta\phi$, respectively. For comparison, the bottom row of each plot shows the difference (PbPb minus pp) of these correlated yields. Measurements of the per-jet invariant track yields show an enhancement of soft particles ($p_{\mathrm{T}}^{\mathrm{trk}} < 3$ GeV) in central PbPb collisions relative to pp, which decreases in more peripheral collisions. The particle yield excess also decreases as a function of $p_{\mathrm{T}}^{\mathrm{trk}}$, such that no significant enhancement is observed in the range $3 < p_{\mathrm{T}}^{\mathrm{trk}} < 8$ GeV.

7.2 Radial distribution of charged-particle yields

Results may also be presented as a function of radial distance from the jet axis $\Delta r = \sqrt{\Delta\eta^2 + \Delta\phi^2}$. Figure 3 presents charged particle yields, differentially in $p_{\mathrm{T}}^{\mathrm{trk}}$, as a function of Δr. For comparison, the bottom row of each plot shows the difference, PbPb minus pp. This shows the particles contributing to a jet fragmentation function measurement within a given radius from a jet, and illustrates the radial dependence of modifications extending to at least $\Delta r = 1$.

7.3 Integrated yields of charged particles

To summarize the magnitude of the modifications to particle yields in PbPb relative to pp colllisions, integrated yields as a function of $p_{\mathrm{T}}^{\mathrm{trk}}$ are presented in Fig. 4. This quantifies the low-p_{T} excess in central PbPb collisions to as many as 4 additional particles (in central PbPb

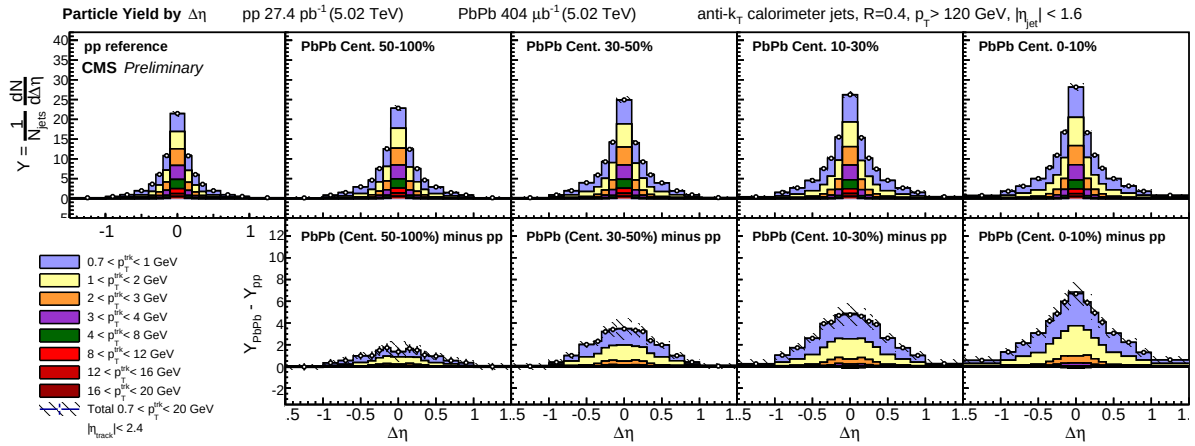

Figure 1: Top row: distributions of charged particle yields correlated to jets with $p_{\mathrm{T}} > 120$ GeV as a function of $\Delta\eta$ (projected over $|\Delta\phi| < 1$), shown differentially for all $p_{\mathrm{T}}^{\mathrm{trk}}$ bins for pp, peripheral PbPb, and central PbPb data. Bottom row: PbPb minus pp difference in these distributions. Hatched lines on $p_{\mathrm{T}}^{\mathrm{trk}}$-inclusive points show total systematic uncertainties.

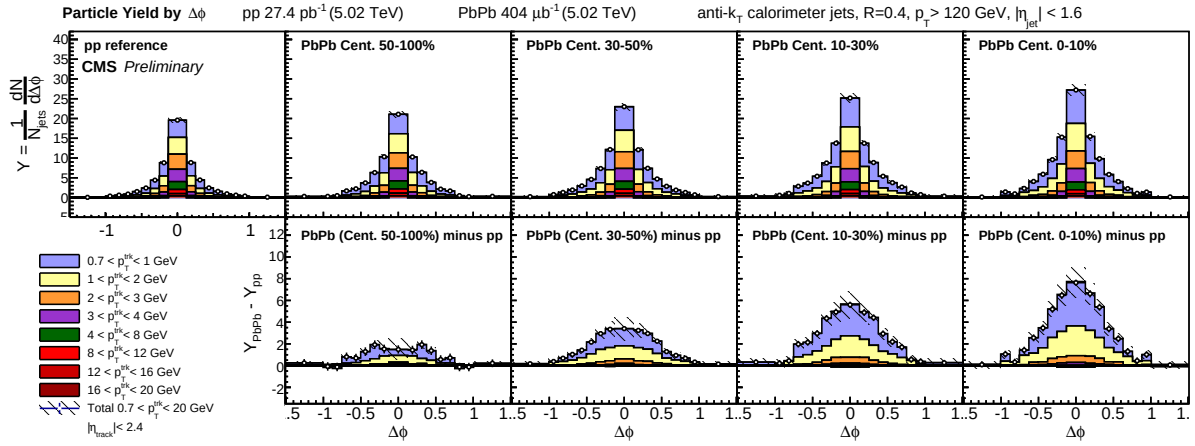

Figure 2: Top row: distributions of charged particle yields correlated to jets with $p_{\mathrm{T}} > 120$ GeV as a function of $\Delta\phi$ (projected over $|\Delta\eta| < 1$), shown differentially for all $p_{\mathrm{T}}^{\mathrm{trk}}$ bins for pp, peripheral PbPb, and central PbPb data. Bottom row: PbPb minus pp difference in these distributions. Hatched lines on $p_{\mathrm{T}}^{\mathrm{trk}}$-inclusive points show total systematic uncertainties.

relative to pp reference) per unit of $p_{\mathrm{T}}^{\mathrm{trk}}$ in the lowest $p_{\mathrm{T}}^{\mathrm{trk}}$ bin. This excess decreases smoothly with $p_{\mathrm{T}}^{\mathrm{trk}}$ in each centrality bin, until the 4–8 GeV central PbPb bin is consistent with or slightly depleted relative to pp reference. For tracks with $p_{\mathrm{T}}^{\mathrm{trk}} > 8$ GeV, there is no evident modification in PbPb compared to pp.

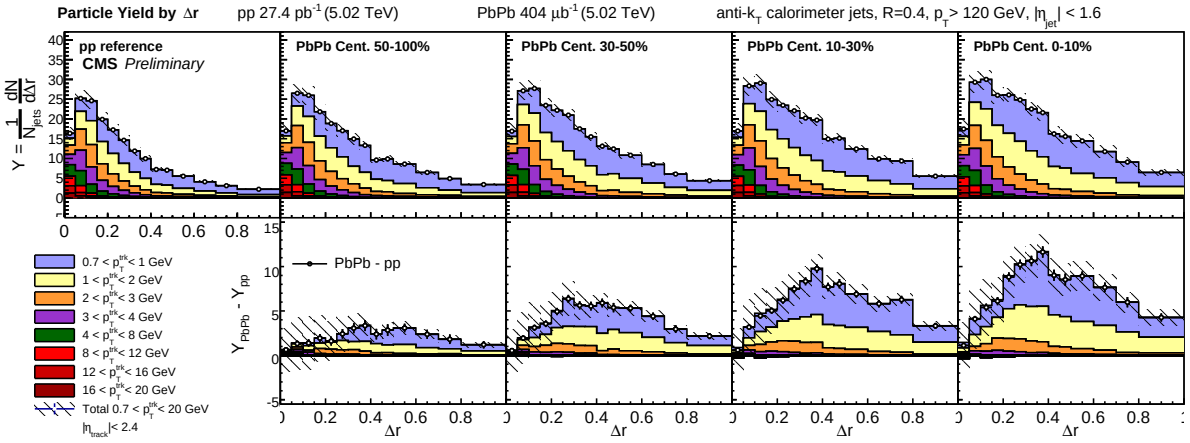

Figure 3: Top row: distributions of charged particle yields correlated to jets with $p_{\mathrm{T}} > 120$ GeV as a function of Δr, shown differentially for all $p_{\mathrm{T}}^{\mathrm{trk}}$ bins. Bottom row: PbPb minus pp difference in these distributions. Hatched lines on $p_{\mathrm{T}}^{\mathrm{trk}}$-inclusive points show total systematic uncertainties.

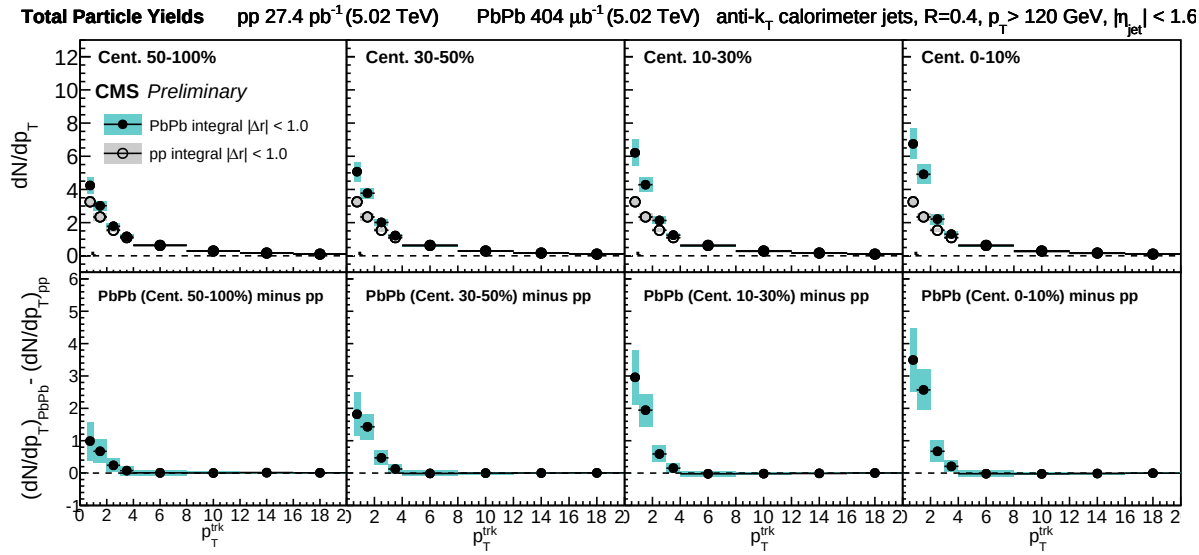

Figure 4: Top row: integrated yields of charged particle yields correlated to jets with $p_{\mathrm{T}} > 120$ GeV as a function of $p_{\mathrm{T}}^{\mathrm{trk}}$ bins for PbPb data, compared to pp reference. Bottom row: integrated excess yield, PbPb minus pp. New measurements of excess yields at 5.02 TeV are compared to those measured at 2.76 TeV in CMS study [12].

7.4 Jet radial transverse momentum profile and jet shapes

By weighting correlations by track p_T on a per-track basis, we obtain distributions of charged-particle p_T relative to the jet axis. After applying an identical procedure of pair-acceptance correction and background subtraction to that used for particle density correlations, these p_T distributions may be used to extract a measurement of jet shape as a function of Δr. In the correlation technique, jet shape $\rho(\Delta r)$ is extracted by integrating 2D jet-peak momentum distributions in annuli with radial width $\delta r = 0.05$, where each has an inner radius of $r_a = \Delta r - \delta r/2$ and an outer radius of $r_b = \Delta r + \delta r/2$. For this measurement, an inclusive high-p_T^{trk} bin is included to capture particles with $20 < p_T^{trk} < 300$ GeV. The resulting transverse momentum profile of the jet is defined as:

$$P(\Delta r) = \frac{1}{\delta r}\frac{1}{N_{jets}}\Sigma_{jets}\Sigma_{tracks\in(r_a,r_b)}p_T^{trk} \tag{4}$$

This profile is then normalized to unity within $\Delta r = 1$ to produce the jet shape $\rho(\Delta r)$:

$$\rho(\Delta r) = \frac{1}{\delta r}\frac{\Sigma_{jets}\Sigma_{tracks\in(r_a,r_b)}p_T^{trk}}{\Sigma_{jets}\Sigma_{tracks}p_T^{trk}} \tag{5}$$

The top row of Fig. 5 presents the jet transverse momentum profile $P(\Delta r)$ in pp and PbPb data, while the middle row shows the jet shape $\rho(\Delta r)$, normalized to unity within $\Delta r = 1$. Here again redistribution of energy from small to large angles from the jet cone is evident in PbPb relative to pp reference, as seen in the dipping then rising trend in the jet shape ratio $\rho(\Delta r)_{PbPb}/\rho(\Delta r)_{pp}$ presented in the bottom row. Note that in comparing this measurement at 5.02 TeV to previous measurements at 2.76 TeV, it is relevant that the pp reference is broader at 5.02 TeV than at 2.76 TeV, likely due to the greater fraction of gluon versus quark jets that pass the kinematic selections of the analysis at the higher center-of-mass energy.

8 Summary

This analysis studies properties of high-p_T jets in heavy ion collisions, using LHC Run-2 data collected by the CMS detector at collision energy $\sqrt{s_{NN}} = 5.02$ TeV in 2015. These studies are based on correlations between jets with $p_T > 120$ GeV, and charged-particle tracks with $0.7 < p_T^{trk} < 300$ GeV, analyzed differentially in p_T^{trk} and collision centrality. Charged-particle correlations are presented as a function of angular distance from the jet, individually $\Delta\eta$ and $\Delta\phi$. In these studies, a low-p_T excess (tracks with $p_T^{trk} < 3$ GeV) extending to large angles $\Delta\eta = 1$ and $\Delta\phi = 1$ is found in central PbPb collisions relative to pp reference. In addition to separate studies in $\Delta\eta$ and $\Delta\phi$, charged-particle densities are also measured as a function of distance from the jet axis Δr. To summarize these measurements, correlations are integrated over $\Delta r < 1$ to obtain a measurement of the total number of particles in each p_T^{trk} class. A comparison of integrals shows as many as three additional low-p_T particles per unit of p_T^{trk} in central PbPb collisions relative to pp reference.

In addition to these charged-particle density studies, correlations are constructed with each track weighted by its p_T^{trk} in order to study the overall distribution of p_T^{trk} with respect to the jet axis. This is used to measure the jet shape $\rho(\Delta r)$ to a distance of $\Delta r = 1$ from the jet axis, presented differentially as a function of p_T^{trk}. A comparison of central PbPb versus pp jet shape shows redistribution of p_T^{trk} from small angles ($\Delta r < 0.3$) near the jet axis to large angles

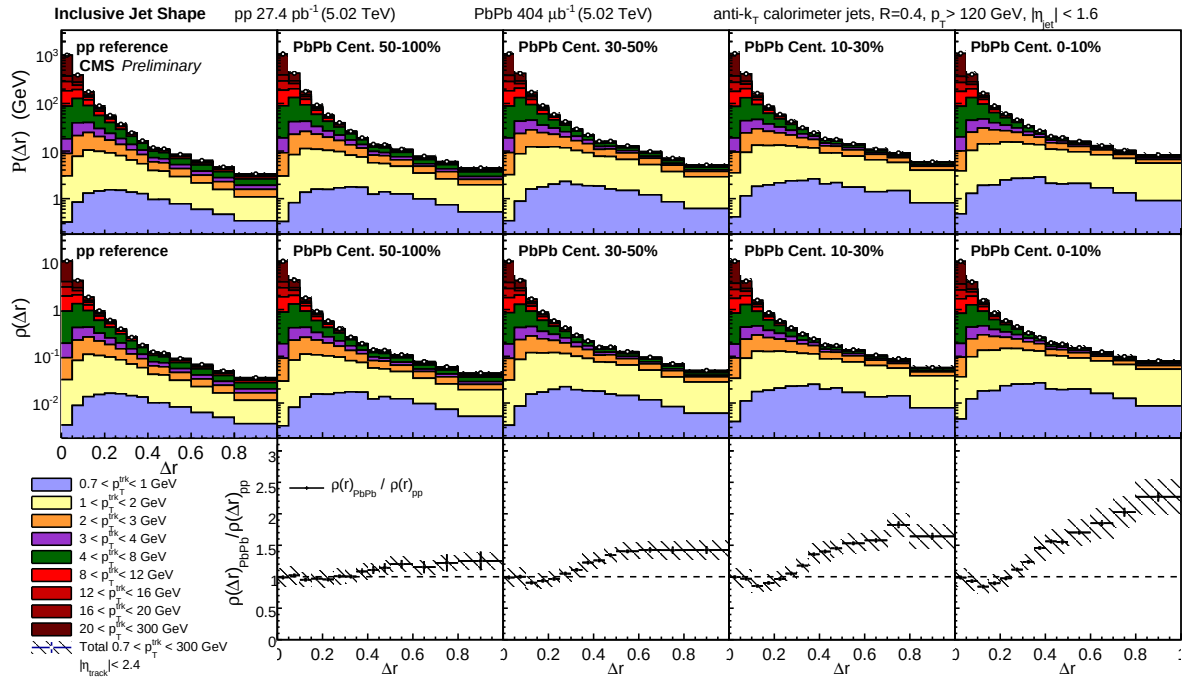

Figure 5: Top row: Transverse momentum profile of jets $\mathrm{P}(\Delta r)$ in pp and PbPb, shown differentially in $p_{\mathrm{T}}^{\mathrm{trk}}$. Middle row: jet shapes $\rho(\Delta r)$ (normalized to unity over $\Delta r < 1$) in PbPb and pp. Bottom row: jet shape ratio $\rho(\Delta r)_{\mathrm{PbPb}}/\rho(\Delta r)_{\mathrm{pp}}$. Hatched lines on $p_{\mathrm{T}}^{\mathrm{trk}}$-inclusive points show total systematic uncertainties.

($\Delta r = 1$) away from the jet axis. In all cases, the modifications observed both in terms of yield modification and jet shapes are similar between the measurements at $\sqrt{s_{\mathrm{NN}}}$ = 2.76 and 5.02 TeV when directly comparing PbPb to pp differences in corresponding centrality bins.

References

[1] J. D. Bjorken, "Energy loss of energetic partons in QGP: possible extinction of high p_{T} jets in hadron-hadron collisions", (1982). FERMILAB-PUB-82-059-THY.

[2] STAR Collaboration, "Direct observation of dijets in central Au+Au collisions at $\sqrt{s_{\mathrm{NN}}}$ = 200 GeV", *Phys. Rev. Lett.* **97** (2006) 162301, doi:10.1103/PhysRevLett.97.162301, arXiv:nucl-ex/0604018.

[3] PHENIX Collaboration, "Transverse momentum and centrality dependence of dihadron correlations in Au+Au collisions at $\sqrt{s_{\mathrm{NN}}}$ = 200 GeV: Jet-quenching and the response of partonic matter", *Phys. Rev. C* **77** (2008) 011901, doi:10.1103/PhysRevC.77.011901, arXiv:0705.3238.

[4] ATLAS Collaboration, "Observation of a Centrality-Dependent Dijet Asymmetry in Lead-Lead Collisions at $\sqrt{s_{\mathrm{NN}}} = 2.76$ TeV with the ATLAS Detector at the LHC", *Phys. Rev. Lett.* **105** (2010) 252303, doi:10.1103/PhysRevLett.105.252303, arXiv:1011.6182.

[5] CMS Collaboration, "Observation and studies of jet quenching in PbPb collisions at $\sqrt{s_{\mathrm{NN}}}$ = 2.76 TeV", *Phys. Rev. C* **84** (2011) 024906, doi:10.1103/PhysRevC.84.024906, arXiv:1102.1957.

[6] CMS Collaboration, "Jet momentum dependence of jet quenching in PbPb collisions at $\sqrt{s_{\mathrm{NN}}} = 2.76$ TeV", *Phys. Lett. B* **712** (2012) 176, doi:10.1016/j.physletb.2012.04.058, arXiv:1202.5022.

[7] ALICE Collaboration, "Measurement of jet suppression in central Pb-Pb collisions at $\sqrt{s_{\mathrm{NN}}}$ = 2.76 TeV", *Phys. Lett. B* **746** (2015) 1, doi:10.1016/j.physletb.2015.04.039, arXiv:1502.01689.

[8] CMS Collaboration, "Measurement of jet fragmentation in PbPb and pp collisions at $\sqrt{s_{\mathrm{NN}}} = 2.76$ TeV", *Phys. Rev. C* **90** (2014) 024908, doi:10.1103/PhysRevC.90.024908, arXiv:1406.0932.

[9] ATLAS Collaboration, "Measurement of inclusive jet charged-particle fragmentation functions in Pb+Pb collisions at $\sqrt{s_{NN}} = 2.76$ TeV with the ATLAS detector", *Phys. Lett.* **B739** (2014) 320–342, doi:10.1016/j.physletb.2014.10.065, arXiv:1406.2979.

[10] CMS Collaboration, "Modification of jet shapes in PbPb collisions at $\sqrt{s_{\mathrm{NN}}} = 2.76$ TeV", *Phys. Lett. B* **730** (2014) 243, doi:10.1016/j.physletb.2014.01.042, arXiv:1310.0878.

[11] CMS Collaboration, "Measurement of transverse momentum relative to dijet systems in PbPb and pp collisions at $\sqrt{s_{\mathrm{NN}}} = 2.76$ TeV", *JHEP* **01** (2016) 6, doi:10.1007/JHEP01(2016)006, arXiv:1509.09029.

[12] CMS Collaboration, "Correlations between jets and charged particles in PbPb and pp collisions at $\sqrt{s_{\mathrm{NN}}} = 2.76$ TeV", *JHEP* **02** (2016) 156, doi:10.1007/JHEP02(2016)156, arXiv:1601.00079.

[13] CMS Collaboration, "Decomposing transverse momentum balance contributions for quenched jets in PbPb collisions at $\sqrt{s_{\mathrm{N\,N}}} = 2.76$ TeV", *JHEP* **11** (2016) 055, doi:10.1007/JHEP11(2016)055, arXiv:1609.02466.

[14] L. Apolinario, N. Armesto, and L. Cunqueiro, "An analysis of the influence of background subtraction and quenching on jet observables in heavy-ion collisions", *JHEP* **02** (2013) 022, doi:10.1007/JHEP02(2013)022, arXiv:1211.1161.

[15] A. Ayala, I. Dominguez, J. Jalilian-Marian, and M. E. Tejeda-Yeomans, "Jet asymmetry and momentum imbalance from $2 \to 2$ and $2 \to 3$ partonic processes in relativistic heavy-ion collisions", *Phys. Rev. C* **92** (2015), no. 4, 044902, doi:10.1103/PhysRevC.92.044902, arXiv:1503.06889.

[16] J.-P. Blaizot, Y. Mehtar-Tani, and M. A. C. Torres, "Angular structure of the in-medium QCD cascade", *Phys. Rev. Lett.* **114** (2015), no. 22, 222002, doi:10.1103/PhysRevLett.114.222002, arXiv:1407.0326.

[17] M. A. Escobedo and E. Iancu, "Event-by-event fluctuations in the medium-induced jet evolution", *JHEP* **05** (2016) 008, doi:10.1007/JHEP05(2016)008, arXiv:1601.03629.

[18] J. Casalderrey-Solana et al., "Angular Structure of Jet Quenching Within a Hybrid Strong/Weak Coupling Model", arXiv:1609.05842.

[19] CMS Collaboration, "The CMS experiment at the CERN LHC", *JINST* **3** (2008) S08004, doi:10.1088/1748-0221/3/08/S08004.

[20] CMS Collaboration, "Determination of Jet Energy Calibration and Transverse Momentum Resolution in CMS", *JINST* **6** (2011) P11002, doi:10.1088/1748-0221/6/11/P11002, arXiv:1107.4277.

[21] CMS Collaboration, "Description and performance of track and primary-vertex reconstruction with the CMS tracker", *JINST* **9** (2014) P10009, doi:10.1088/1748-0221/9/10/P10009, arXiv:1405.6569.

[22] T. Sjöstrand, S. Mrenna, and P. Skands, "PYTHIA 6.4 physics and manual", *JHEP* **05** (2006) 026, doi:10.1088/1126-6708/2006/05/026, arXiv:hep-ph/0603175.

[23] GEANT4 Collaboration, "GEANT4–a simulation toolkit", *Nucl. Instrum. and Methods A* **506** (2003) 250, doi:10.1016/S0168-9002(03)01368-8.

[24] I. P. Lokhtin and A. M. Snigirev, "A model of jet quenching in ultrarelativistic heavy ion collisions and high-p_{T} hadron spectra at RHIC", *Eur. Phys. J. C* **45** (2006) 211, doi:10.1140/epjc/s2005-02426-3, arXiv:hep-ph/0506189.

[25] M. Cacciari, G. P. Salam, and G. Soyez, "FastJet user manual", *Eur. Phys. J. C* **72** (2012) 1896, doi:10.1140/epjc/s10052-012-1896-2, arXiv:1111.6097.

[26] O. Kodolova, I. Vardanian, A. Nikitenko, and A. Oulianov, "The performance of the jet identification and reconstruction in heavy ions collisions with CMS detector", *Eur. Phys. J. C* **50** (2007) 117, doi:10.1140/epjc/s10052-007-0223-9.

[27] CMS Collaboration, "Study of high-p_{T} charged particle suppression in PbPb compared to pp collisions at $\sqrt{s_{\mathrm{NN}}} = 2.76$ TeV", *Eur. Phys. J. C* **72** (2012) 1945, doi:10.1140/epjc/s10052-012-1945-x, arXiv:1202.2554.

[28] CMS Collaboration, "Observation of long-range, near-side angular correlations in proton-proton collisions at the LHC", *JHEP* **09** (2010) 091, doi:10.1007/JHEP09(2010)091, arXiv:1009.4122.

[29] CMS Collaboration, "Long-range and short-range dihadron angular correlations in central PbPb collisions at $\sqrt{s_{\mathrm{NN}}}$ = 2.76 TeV", *JHEP* **07** (2011) 076, doi:10.1007/JHEP07(2011)076, arXiv:1105.2438.

[30] CMS Collaboration, "Observation of long-range, near-side angular correlations in pPb collisions at the LHC.", *Phys. Lett. B* **718** (2013) 795, doi:10.1016/j.physletb.2012.11.025, arXiv:1210.5482.

[31] CMS Collaboration, "Multiplicity and transverse momentum dependence of two- and four-particle correlations in pPb and PbPb collisions", *Phys. Lett. B* **724** (2013) 213, doi:10.1016/j.physletb.2013.06.028, arXiv:1305.0609.

[32] CMS Collaboration, "Measurement of jet fragmentation into charged particles in pp and PbPb collisions at $\sqrt{s_{\mathrm{NN}}} = 2.76$ TeV", *JHEP* **10** (2012) 087, doi:10.1007/JHEP10(2012)087, arXiv:1205.5872.